Kinetostatic Modeling and Position-Orientation Control of Bellow-Shaped Soft Continuum Robots

Yu Rong and Guoying Gu, *Senior Member, IEEE*

***Abstract*—Bellow-shaped soft continuum robots with parallel mechanisms feature an excellent balance between structural stiffness and contact compliance, making them highly promising in various applications. However, their complex structures and nonlinear elastic characteristics pose significant challenges in modeling and control. In this work, we propose a kinetostatic model and a corresponding position-orientation controller for bellow-shaped soft continuum robots. First, bellow-shaped soft actuators are simplified into hyperelastic cylinder soft actuators with mechanical equivalence. In addition, the overall deformation is decoupled into elongation and bending components to enhance computational efficiency. Based on these two simplifying strategies, the kinetostatic model is developed with absolute nodal coordinate formulation theory. Then, forward and inverse kinetostatic mappings are defined, and the numerical solution algorithm is presented. Finally, the developed model is experimentally validated through configuration simulation and feedforward trajectory tracking. Experimental results demonstrate that the developed model achieves low prediction errors, with configuration simulation errors of 3.43%. Furthermore, with the model-based feedforward controller, a two-segment soft continuum robot can accurately follow desired trajectories with specified bending angles, achieving average position and angle errors of 4.14 mm and 1.58°, respectively.**

***Index Terms*—Absolute nodal coordinate formulation (ANCF), kinetostatic model, position and orientation control, soft continuum robot.**

I. Introduction

PNEUMATIC soft continuum robots made from low-modulus materials feature light weight, low inertia, high flexibility, and superior compliance compared to rigid-bodied robots [1], [2]. These advantages contribute to their extensive applications in various fields, such as assistive rehabilitation devices [3], [4], [5], [6], [7]; environment exploration [8], [9]; and minimally invasive surgery [10]. However, the inherent compliance also results in issues of low stiffness and limited load capacity.

To increase the stiffness without compromising compliance, several strategies have been explored. Inspired by rigid parallel robots, parallel mechanisms are introduced to design soft continuum robots [11], [12]. By connecting multiple slender soft actuators between a base and a platform, the aspect ratio of soft continuum robots is reduced, thereby improving the structural stiffness. In addition, bellow-shaped soft actuators made from high-modulus materials have been employed to further increase stiffness [13]. However, the closed kinematic chains and complex deformation of retractable folds both present significant challenges in modeling and controlling, particularly in scenarios where simplified models and feedback controllers are impractical [14], [15], [16], [17].

Considering complex structures and designs of bellow-shaped soft continuum robots, finite element method (FEM) is the mostly widespread modeling method [18], [19]. In FEM, soft continuum robots are discretized into numerous elements, resulting in high-dimensional motion equations. This characteristic inherently increases the computational burden and the time required to achieve a converged solution. Furthermore, most degrees of freedom in an FEM-based model are redundant for control tasks. Therefore, it is challenging to design efficient controllers with FEM-based models.

To improve the computational efficiency, various geometrical models have been proposed. These models focus solely on describing deformed backbones of soft continuum robots. Based on this simplification approach, deformed backbones are then parameterized by geometrical curves, such as piecewise constant curvature (PCC) arcs [20], [21], Euler spiral curves [22], and Pythagorean hodograph curves [23]. However, PCC models are primarily kinematic and do not account for external forces, leading to limited applications. Although variable curvature models achieve high tracking accuracy with low computational

Received 4 July 2025; revised 14 October 2025; accepted 27 December 2025. Recommended by Technical Editor P. Mani Pathak and Senior Editor K. Oldham. This work was supported in part by the National Natural Science Foundation of China under Grant T2293725 and Grant 52025057, in part by the Science and Technology Commission of Shanghai Municipality under Grant 24511103400, in part by the State Key Laboratory of Mechanical System and Vibration under Grant MSVZD202401, and in part by Xplorer Prize. *(Corresponding author: Guoying Gu.)*

The authors are with the State Key Laboratory of Mechanical System and Vibration, School of Mechanical Engineering, Shanghai Jiao Tong University, Shanghai 200240, China, and also with the Shanghai Key Laboratory of Intelligent Robotics, Shanghai Jiao Tong University, Shanghai 200240, China (e-mail: rongyu@sjtu.edu.cn; guguoying@sjtu.edu.cn).

This article has supplementary material provided by the authors and color versions of one or more figures available at https://doi.org/10.1109/TMECH.2026.3650845.

Digital Object Identifier 10.1109/TMECH.2026.3650845

cost [23], they are generally designed for single-segment soft continuum robots, which exhibit restricted workspace and flexibility. Nevertheless, such geometrical model is only valid for a specific class of soft continuum robots under certain working conditions. Moreover, geometrical models are primarily kinematic models without considering external forces, limiting the realistic applications.

Besides geometrical models, continuum mechanics models are also proposed to simulate and control soft continuum robots. According to applied kinematic models, continuum mechanics models can be classified into continuous models and discrete models. For continuous models, Cosserat rod models [24], Euler-Bernoulli beam models [25], and Kirchhoff beam models [26] are representative examples. Various discretization algorithms, such as the Ritz method [27], [28], are employed to calculate the controlling pressure based on these models. The implementation of continuous models normally relies on assumptions of rigid cross-sections, linear elastic relations, and analytical equations of actuation forces. However, for bellow-shaped soft robots, cross-sectional shapes inevitably change during the deformation process, and force-displacement relationships are typically nonlinear. These facts greatly limit the application of continuous models in modeling and controlling bellow-shaped soft continuum robots.

Alternatively, the ANCF model, as a representative discrete model, has recently emerged for modeling soft robots. ANCF models discretize soft continuum robots into several elements. The displacement strain field of each element is parameterized by the global positions and the position gradients of nodes [29], [30]. In our previous work, we have used the ANCF model for modeling and controlling soft parallel robots with high computational efficiency [11]. However, this method requires the explicit equation of actuation forces and constant structural stiffness, which are unavailable for modeling and controlling bellow-shaped soft robots.

In this article, we extend the ANCF model for the kinetostatic model of bellow-shaped soft continuum robots, which considers the nonlinear elasticity and avoids the explicit equation of actuation forces. To this end, bellow-shaped soft actuators are first simplified into hyperelastic cylinder soft actuators with equivalent mechanical parameters. Then, the overall configuration deformation is divided into the elongation deformation and the bending deformation. With these two simplifying approaches, the kinetostatic model is developed based on the ANCF theory. Afterwards, the mappings between the actuator space and the configuration space are established using the kinetostatic model. To determine equivalent mechanical parameters, a series of parameter identification experiments are designed and conducted. Finally, the developed model is experimentally validated through configuration simulation and feedforward trajectory tracking control. Experimental results show that the kinetostatic model accurately predicts deformed configurations with different loads and vertical stiffness with different actuation pressures. Moreover, the simultaneous control of the end position and the orientation is realized with the developed model.

The contributions of this work are summarized as follows.

1) We propose a kinetostatic model for bellow-shaped soft continuum robots based on the ANCF theory. Two theoretical modifications are introduced to make ANCF theory feasible for modeling bellow-shaped soft robots.
2) We define the forward and inverse kinetostatic problems. Then, the mathematical equations are presented, and their numerical algorithms are developed.
3) We apply the developed model for configuration simulation and feedforward trajectory tracking. Experimental results well demonstrate the advancements of the developed model.

The rest of this article is organized as follows. In Section II, the design and fabrication of the bellow-shaped soft continuum robot are introduced. Section III presents the kinetostatic model based on the ANCF theory. In Section IV, the forward and inverse kinetostatic problems are defined, and then the numerical calculation algorithm is developed. Sections V and VI present parameter identification experiments and validation experiments, respectively. Finally, Section VII concludes this article.

II. Design and Fabrication

In this section, the design and fabrication process of a one-segment soft continuum robot are presented. As illustrated in Fig. 1(a), the fabrication process involves two steps.

Step 1: The bellow-shaped soft actuators are fabricated by the vacuum casting method with the hyperelastic material DPI8400 (Shore 50 A). Then, the bellow-shaped soft actuator is sealed with two resin caps using silicon adhesive (Sil-Poxy, Smooth-on, USA).

Step 2: Three soft actuators are evenly distributed around the central axis, and their ends are fixed on two base plates. Then, two resin caps and soft actuators are bonded together to provide support for soft actuators, making them less prone to elastic instability. Meanwhile, this approach can prevent bulking and collisions of soft actuators by localizing deformation to the unbonded parts of soft actuators. Therefore, modeling and control accuracy are enhanced.

The geometric dimensions of the bellow-shaped actuator are shown in Fig. 1(b). Each soft actuator can be actuated by either positive or negative pressure. By varying the combination of actuation pressures, the one-segment soft continuum robot can exhibit elongation, contraction, and bending deformation.

III. Kinetostatic Model

In this section, modeling simplifications and assumptions of a soft actuator are first introduced. Then, ANCF-based kinematics of a variable curvature soft actuator is presented. Based on this configuration parameterization method, the kinetostatic model is derived. Moreover, boundary conditions are also introduced and mathematically expressed. Finally, explicit model equations comprising both the kinetostatic model and boundary conditions are derived.

A. Modeling Simplification

First, a bellow-shaped soft actuator is simplified as a hyperelastic cylinder soft actuator [as shown in Fig. 2(a)]. To guarantee the model accuracy, the cylinder soft actuator should

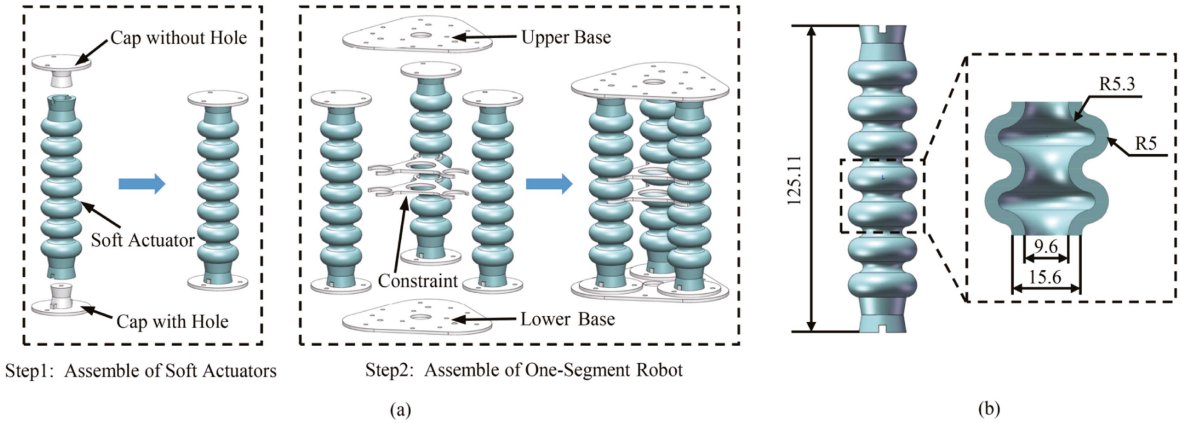

Fig. 1. Fabrication and design of the one-segment soft continuum robot. (a) Fabrication process of one segment soft continuum robot. *Step 1:* The bellow-shaped actuator is sealed by two resin caps. *Step 2:* Three soft actuators, two bases, and two constraints are assembled into a one-segment soft continuum robot. (b) Geometric dimension of the bellow-shaped actuator (Unit: mm).

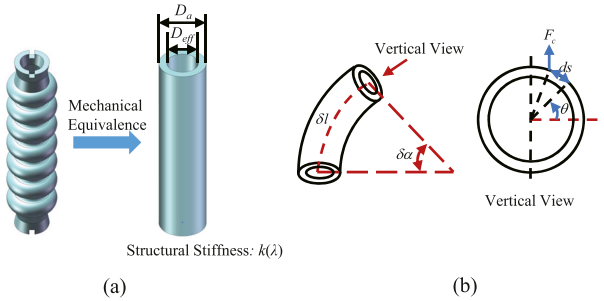

Fig. 2. (a) Bellow-shape actuator is mechanically equivalent to a hyperelastic cylinder soft actuator with three equivalent parameters (i.e., the nonlinear structural stiffness $k(\lambda)$, the effective actuation diameter D_{eff}, and the cross-sectional diameter D_a). (b) Schematic illustration of the distribution of bending forces.

be mechanically equivalent to the bellow-shaped soft actuator. Therefore, three equivalent mechanical parameters (i.e., the nonlinear structural stiffness $k(\lambda)$ related to the stretch ratio λ, the effective actuation diameter D_{eff}, and the cross-sectional diameter D_a) are used. Furthermore, the tensile stiffness k_t and the bending stiffness k_b can be expressed by these equivalent mechanical parameters.

For a soft actuator with an undeformed length l_0, the structural stiffness $k(\lambda)$, and the tensile stiffness k_t are defined by

$$F_t = k\left(\lambda\right)\Delta l, \frac{F_t}{k_t} = \frac{\Delta l}{l_0} \tag{1}$$

where F_t and Δl are the tensile force and the length change, respectively. Then, the tensile stiffness and the structural stiffness satisfy

$$k_t = k\left(\lambda\right) l_0. \tag{2}$$

The relation between the bending stiffness k_b and equivalent mechanical parameters can be derived by considering the moment balance on an infinitesimal slice of the soft actuator. For the slice with the undeformed length δl_0, the strain ratio and the bending angle are denoted as λ and $\delta\alpha$, respectively. The definition of the bending stiffness is given by $M/k_b = \delta\alpha/\delta l$, where M and δl are the moment and the deformedlength, respectively. As illustrated in Fig. 2(b), the moment M can be calculated by (see Supplementary Material for further details)

$$M = \int_{\partial C} F_c \frac{D_a}{2}\cos\theta = \frac{D_a^2 l_0 \lambda k\left(\lambda\right)}{8}\frac{\delta\alpha}{\delta l}. \tag{3}$$

Thus, the bending stiffness k_b can be written as

$$k_b = M\frac{\delta l}{\delta\alpha} = \frac{D_a^2 l_0 \lambda k\left(\lambda\right)}{8}. \tag{4}$$

Except for the mechanical simplification, we also make following assumptions to further facilitate the modeling process.

1) The length and radial dimensions of the bellow-shaped soft actuator are approximately constant when the actuation pressure remains constant. It implies that the volume of the soft actuator's chamber stays nearly constant.
2) The effective actuation diameter remains constant during deformation.
3) The cross-sectional diameter remains constant during deformation.
4) Three soft actuators constituting a one-segment soft continuum robot are identical.

Assumption 1 is validated by previous researches with the FEM method [18], [19], [31]. Assumption 2 is verified by the parameter identification experiment, which will be presented in Section V. Assumption 3 is also reasonable because the diameter changes in the convex and concave regions are opposite during deformation, making the effective diameter approximately unchanged.

B. Kinematics

To parameterize the variable curvature configuration of the soft actuator, the gradient deficient ANCF method is employed [32], [33]. In this method, each soft actuator is discretized into n elements by $n+1$ nodes, which are set along its backbone. As shown in Fig. 3, for the ith element with original length l, the states are parameterized by a reference arc length

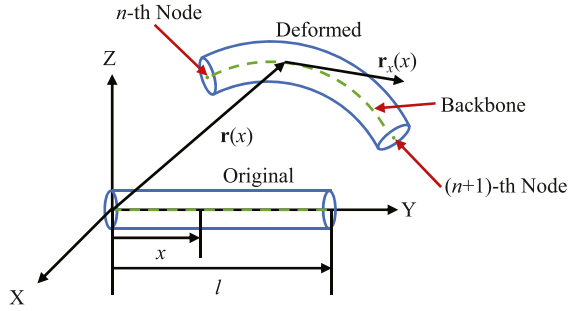

Fig. 3. Schematic illustration of the configuration parameterization of a variable curvature soft actuator based on the ANCF method.

parameter $x \in [0, l]$. Then, the global position of an arbitrary point $\mathbf{r}(x) \in \mathbb{R}^3$ is defined as a function of the reference arc length parameter. Besides, the position gradient of an arbitrary point $\mathbf{r}_x(x) \in \mathbb{R}^3$ is also adopted to describe the rotation motion, where $(\cdot)_x$ denotes the derivative with respect to x. These two vectors define the vector of nodal coordinates as

$$\mathbf{q}(x) = \begin{bmatrix} \mathbf{r}^T(x) & \mathbf{r}_x^T(x) \end{bmatrix}^T \in \mathbb{R}^6. \tag{5}$$

Using the ith nodal coordinates $\mathbf{q}_i^T$ and $(i+1)$th nodal coordinates $\mathbf{q}_{i+1}^T$, the global displacement field of the ith element $\mathbf{r}(x)$ can be given by

$$\mathbf{r}(x) = \mathbf{S}(x)\mathbf{q}^i \tag{6}$$

where $\mathbf{S}(x) \in \mathbb{R}^{3\times 12}$ is the shape function and $\mathbf{q}^i = \begin{bmatrix} \mathbf{q}_i^T & \mathbf{q}_{i+1}^T \end{bmatrix}^T$. The explicit expression of $\mathbf{S}(x)$ is expressed as

$$\begin{aligned} &\mathbf{S}(x) = \begin{bmatrix} s_1\mathbf{I}_3 & s_2\mathbf{I}_3 & s_3\mathbf{I}_3 & s_4\mathbf{I}_3 \end{bmatrix} \\ &\begin{cases} s_1 = 1 - 3\xi^2 + 2\xi^3 \\ s_2 = l\left(\xi - 2\xi^2 + \xi^3\right) \\ s_3 = 3\xi^2 - 2\xi^3 \\ s_4 = l\left(-\xi^2 + \xi^3\right) \end{cases} \end{aligned} \tag{7}$$

where $\xi = x/l$ and $\mathbf{I}_3$ is a 3×3 identity matrix. Based on this parameterization method, the Green strain tensor $\epsilon(x)$ and the curvature $\kappa(x)$ along the ith element can defined as

$$\begin{cases} \varepsilon(x) = \frac{1}{2}\left(\mathbf{r}_x^T\mathbf{r}_x - 1\right) \\ \kappa(x) = \frac{\|\mathbf{r}_x \times \mathbf{r}_{xx}\|}{\|\mathbf{r}_x\|^3} \end{cases} \tag{8}$$

where $(\cdot)_{xx}$ denotes the second derivative with respect to x. By combining the nodal coordinates of all soft actuators, the nodal coordinate of a soft actuator $\mathbf{q} \in \mathbb{R}^{n_q}$ is given as

$$\mathbf{q} = \begin{bmatrix} q_1 & q_2 & \cdots & q_{n_q-1} & q_{n_q} \end{bmatrix}^T. \tag{9}$$

C. Kinetostatic Model

According to assumption 1, the deformation of the soft continuum robot can be divided into two stages: 1) the internal pressure drives each soft actuator to elongate or contract and 2) the closed kinematic chain enforces actuators to bend.

In the first stage, the mechanical equation of one soft actuator involves the pressure-related force F_p, the deformation-related force F_d, and the external force F_e, which is given as

$$F_p - F_d - F_e = \frac{\pi}{4}\mathrm{PD}_{\mathrm{eff}}^2 - k\left(\lambda\right)\left(\lambda - 1\right)l_0 - F_e = 0. \tag{10}$$

After solving (10), the stretch ratio λ is obtained. The length of the ANCF element changes from l_0 to l, which equals λl_0.

In the second stage, the length remains approximately constant according to assumption 1, which implies $||\mathbf{r}_x(x)|| \approx 1$. Under this circumstance, the curvature $\kappa(x)$ in (8) can be simplified as

$$\kappa(x) = \|\mathbf{r}_{xx}\|. \tag{11}$$

Moreover, the work done by the actuation pressure can be neglected since the volume of the soft actuator's chamber remains nearly constant. For the ith element, according to the principle of virtual work, the generalized external forces equal the generalized internal forces [11], [34]

$$\mathbf{Q}_e^i - \mathbf{Q}_g^i - \mathbf{Q}_f^i = \mathbf{0} \tag{12}$$

where $\mathbf{Q}_e^i$, $\mathbf{Q}_g^i$, and $\mathbf{Q}_f^i$ are the generalized elastic forces, the generalized gravitational forces, and the generalized external forces, respectively.

For the concentrated force $\mathbf{F}$ applied at x_p, the corresponding virtual work is

$$\delta W_f^i = \mathbf{F}^T\delta\mathbf{r}\left(x_p\right) = \mathbf{F}^T\mathbf{S}\left(x_p\right)\delta\mathbf{q}^i. \tag{13}$$

The generalized external force is the variation of the work done by the concentrated force, which is expressed by

$$\mathbf{Q}_f^i = \left(\frac{\partial W_f^i}{\partial \mathbf{q}^i}\right)^T = \mathbf{S}^T\left(x_p\right)\mathbf{F}. \tag{14}$$

For the evenly distributed gravitational force, the corresponding virtual work is

$$\delta W_g^i = \int_0^l (\rho\mathbf{g})^T\delta\mathbf{r}(x)dx = \int_0^l (\rho\mathbf{g})^T\mathbf{S}(x)\delta\mathbf{q}^i dx \tag{15}$$

where ρ is the linear density of the deformed soft actuator and $\mathbf{g}$ is the gravitational acceleration. It should be noted that the linear density is a function of the strain ratio λ, equaling the original linear density ρ_0 divided by λ. Based on (15), the generalized gravitational force is calculated as

$$\mathbf{Q}_g^i = \left(\frac{\partial W_g^i}{\partial \mathbf{q}^i}\right)^T = \rho\int_0^l \mathbf{S}^T(x)\mathbf{g}dx. \tag{16}$$

The generalized elastic force is the variation of the total elastic potential energy with respect to the nodal coordinates. The linear constitutive law is adopted to calculate the total elastic potential energy since the tensile strain is small in the second stage. Therefore, the total elastic potential energy is

$$W_e^i = \frac{1}{2}\int_0^l \left(k_t\varepsilon^2 + k_b\kappa^2\right)dx. \tag{17}$$

The independent variable x is omitted here for the sake of concisely. Then, the generalized elastic force can be calculated

as

$$\mathbf{Q}_e^i = \left(\frac{\partial W_e^i}{\partial \mathbf{q}^i}\right)^T = \int_0^l \left(k_t \varepsilon \mathbf{S}_x^T \mathbf{S}_x + k_b \mathbf{S}_{xx}^T \mathbf{S}_{xx}\right) \mathbf{q}^i dx. \quad (18)$$

The detailed expression of $\mathbf{S}_x$ and $\mathbf{S}_{xx}$ are presented in Supplementary Material.

The nodal coordinate of the ith element $\mathbf{q}^i$ and the nodal coordinate of the soft continuum robot $\mathbf{q}$ satisfy

$$\mathbf{q}^i = \mathbf{B}^i \mathbf{q} \quad (19)$$

where $\mathbf{B}^i \in \mathbb{R}^{12 \times n_q}$ is the Boolean matrix. Using the Boolean matrix, the kinetostatic model of the soft actuator in the second stage can be expressed as

$$\mathbf{Q}_e - \mathbf{Q}_g - \mathbf{Q}_f = \mathbf{0} \quad (20)$$

where

$$\mathbf{Q}_e = \sum_i (\mathbf{B}^i)^T \mathbf{Q}_e^i, \mathbf{Q}_g = \sum_i (\mathbf{B}^i)^T \mathbf{Q}_g^i, \mathbf{Q}_f = \sum_i (\mathbf{B}^i)^T \mathbf{Q}_f^i. \quad (21)$$

D. Boundary Conditions

The closed kinematic chains introduce geometric constraints, which are considered boundary conditions during the computation process. There are two types of boundary conditions: plane boundary conditions and connection boundary conditions.

1) Plane Boundary Conditions: Platform boundary conditions arise from two resin constraints and two bases. In these planes, the distance between any two soft actuators remains constant. Besides, the position gradient of each soft actuator should be perpendicular to the plane. The global position and position gradient of the ith ($i = 1, 2, 3$) soft actuator are denoted as $\mathbf{r}_i$ and $\mathbf{r}_{xi}$, respectively. The distance between any two soft actuators is denoted as d. Then, the plane boundary conditions can be expressed as

$$\begin{cases} (\mathbf{r}_i - \mathbf{r}_j)^T (\mathbf{r}_i - \mathbf{r}_j) - d^2 = 0 \\ \left(\mathbf{r}_{xi}^T \mathbf{r}_{xj}\right)^2 - \|\mathbf{r}_{xi}\|^2 \|\mathbf{r}_{xj}\|^2 = 0 \\ \mathbf{r}_{xi}^T (\mathbf{r}_i - \mathbf{r}_j) = 0. \end{cases} \quad (22)$$

2) Connection Boundary Conditions: For a two-segment soft continuum robot, the middle part between two one-segment soft robots is viewed as a rigid body composed of a single ANCF element with two nodes. This connection between the rigid body and the soft continuum robot introduces connection boundary conditions. Specifically, the global positions of two connected nodes should be identical. In addition, the angle between the position gradients of two connected nodes should remain constant during the computation process. The nodal coordinates of the rigid body and the one-segment soft continuum robot are denoted as $[\mathbf{r}_r, \mathbf{r}_{rx}]$ and $[\mathbf{r}_s, \mathbf{r}_{sx}]$, respectively. The first subscript (i.e., r or s) refers to the rigid section or the soft section. Then, connection boundary conditions are expressed as

$$\begin{cases} \mathbf{r}_r - \mathbf{r}_s = \mathbf{0}_3 \\ \left(\mathbf{r}_{rx}^T \mathbf{r}_{sx}\right)^2 - \left(\|\mathbf{r}_{rx}\| \|\mathbf{r}_{sx}\| \cos\theta\right)^2 = 0 \end{cases} \quad (23)$$

where $\mathbf{0}_3$ represents a three-dimensional zero vector and θ is the constant angle between two position gradients.

E. Explicit Model Equations

According to the above development, we can obtain the entire kinetostatic model of the one-segment or two-segment soft continuum robot with two sets of vector equations.

The first set of vector equations is related to the elongation deformation of each soft actuator, expressed as

$$\frac{\pi}{4} P_i D_{\text{eff}}^2 - k(\lambda_i)(\lambda_i - 1) l_0 - F_{ei} = 0 \quad (24)$$

where the subscript i refers to the ith soft actuator.

The second set of vector equations is related to the bending deformation of each soft actuator driven by the closed kinematic chain. By stacking mechanical equilibrium equations of all soft actuators into a vector $\mathbf{Q} \in \mathbb{R}^{n_q}$ and all boundary conditions into a vector $\mathbf{C} \in \mathbb{R}^{n_c}$, the second set of vector equations can be presented as

$$\begin{cases} \mathbf{Q}(\mathbf{q}, \boldsymbol{\lambda}) + \mathbf{C}_{\mathbf{q}}^T(\mathbf{q}) \boldsymbol{\alpha} = \mathbf{0} \\ \mathbf{C}(\mathbf{q}) = \mathbf{0} \end{cases} \quad (25)$$

where $\boldsymbol{\alpha} \in \mathbb{R}^{n_c}$ is the vector of Lagrange multipliers and $\mathbf{C}_{\mathbf{q}} \in \mathbb{R}^{n_c \times n_q}$ is the Jacobian matrix of the constraint vector with respect to the nodal coordinates.

IV. Forward and Inverse Kinetostatic Problems

In this section, forward and inverse kinetostatic problems are first defined. Then, their equations and numerical algorithm are presented.

A. Definition

The relationship between the actuation pressures $\mathbf{P}$ and the nodal coordinates $\mathbf{q}$ is described by (24) and (25). Based on these equations, both the forward and inverse kinetostatic problems can be defined. Specifically, the forward kinetostatic problem (i.e., the simulation task) refers to solving the nodal coordinates $\mathbf{q}$ and the Lagrange multipliers $\boldsymbol{\alpha}$ given the actuation pressures $\mathbf{P}$. In contrast, the inverse kinetostatic problem (i.e., the motion control task) aims to solve the actuation pressures $\mathbf{P}$, the nodal coordinates $\mathbf{q}$, and the Lagrange multipliers $\boldsymbol{\alpha}$ given the desired target $\mathbf{q}_d$.

B. Forward Kinetostatic Problem

Using (24), the stretch ratios $\boldsymbol{\lambda}$ can be calculated when the actuation pressures $\mathbf{P}$ are known. Therefore, the kinetostatic model of (25) is a system of $n_q + n_c$ residual equations $\mathbf{r}$ with $n_q + n_c$ unknown variables $\mathbf{u} = [\mathbf{q}^T, \boldsymbol{\alpha}^T]^T$. The equations can be numerically solved by the Levenberg–Marquardt algorithm [35] given the initial guess of all unknown variables, which is described in Supplementary Material. In each step, the unknown variables are updated in iterative the form of

$$\mathbf{u}_{k+1} = \mathbf{u}_k - \left(\mathbf{J}_k^T \mathbf{J}_k + \mu \mathbf{I}\right)^{-1} \mathbf{J}_k^T \mathbf{r}_k \quad (26)$$

where k is the iteration number and μ is the damping parameter. $\mathbf{J} = \partial \mathbf{r}/\partial \mathbf{u}$ is the Jacobian matrix given by

$$\mathbf{J} = \begin{bmatrix} \frac{\partial \mathbf{Q}}{\partial \mathbf{q}} + \frac{\partial \left(\mathbf{C}_{\mathbf{q}}^T \boldsymbol{\alpha}\right)}{\partial \mathbf{q}} & \mathbf{C}_{\mathbf{q}}^T \\ \mathbf{C}_{\mathbf{q}} & \mathbf{0}_{n_c \times n_c} \end{bmatrix}. \tag{27}$$

The detailed expression of (27) is presented in Supplementary Material.

C. Inverse Kinetostatic Problem

For the one-segment soft continuum robot, the desired target $\mathbf{q}_d \in \mathbb{R}^3$ is typically the desired end-effector position $\mathbf{q}_p \in \mathbb{R}^3$. For the two-segment soft continuum robot, the desired target $\mathbf{q}_d \in \mathbb{R}^6$ is typically the desired end-effector position $\mathbf{q}_p \in \mathbb{R}^3$ and the desired orientation of the local z-axis $\mathbf{q}_r \in \mathbb{R}^3$. It should be noted that the end-effectors on this kind of two-segment soft continuum robots only have 5 degrees-of-freedom [36]. Thus, it is only possible to simultaneously control the end-effector position and the orientation of one local axis. To realize the motion control task, additional objective equations $\mathbf{O}$ are defined by

$$\begin{aligned} &\mathbf{O} = \mathbf{q}_{ep} - \mathbf{q}_p, \text{ for one-segment soft robots} \\ &\mathbf{O} = \begin{bmatrix} \mathbf{q}_{ep} - \mathbf{q}_p \\ \gamma \left(\mathbf{q}_{er} - \mathbf{q}_r\right) \end{bmatrix}, \text{ for two-segment soft robots} \end{aligned} \tag{28}$$

where $\mathbf{q}_{ep}$ and $\mathbf{q}_{er}$ are the end-effector position and the orientation of the local z-axis. The constant scalar γ is used to nondimensionalize the residual elements. By combining (25) and (28), the residual equations of the inverse kinetostatic problem $\mathbf{r} \in \mathbb{R}^{n_q+n_c+n_o}$ can be written as

$$\mathbf{r} = \begin{bmatrix} \mathbf{Q}\left(\mathbf{q}, \boldsymbol{\lambda}\right) + \mathbf{C}_{\mathbf{q}}^T\left(\mathbf{q}\right)\boldsymbol{\alpha} \\ \mathbf{O}\left(\mathbf{q}\right) \\ \mathbf{C}\left(\mathbf{q}\right) \end{bmatrix} = \mathbf{0} \tag{29}$$

where n_o is the dimension of the objective equations. The vector of unknown variables is $\mathbf{u} = [\boldsymbol{\lambda}^T, \mathbf{q}^T, \boldsymbol{\alpha}^T]^T \in \mathbb{R}^{n_q+n_c+n_o}$. These equations can also be numerically solved by the Levenberg–Marquardt algorithm. The Jacobian matrix $\mathbf{J}$ of each updating iteration is

$$\mathbf{J} = \begin{bmatrix} \frac{\partial \mathbf{Q}}{\partial \boldsymbol{\lambda}} & \frac{\partial \mathbf{Q}}{\partial \mathbf{q}} + \frac{\partial \left(\mathbf{C}_{\mathbf{q}}^T \boldsymbol{\alpha}\right)}{\partial \mathbf{q}} & \mathbf{C}_{\mathbf{q}}^T \\ \mathbf{0}_{n_o \times n_o} & \mathbf{O}_{\mathbf{q}} & \mathbf{0}_{n_o \times n_c} \\ \mathbf{0}_{n_c \times n_o} & \mathbf{C}_{\mathbf{q}} & \mathbf{0}_{n_c \times n_c} \end{bmatrix}. \tag{30}$$

The detailed expression of (30) is presented in Supplementary Material. After solving the vector of stretch ratios, the actuation pressures can be calculated by (24).

V. Parameter Identification

In this section, a series of parameter identification experiments are designed and conducted.

A. Identification of Structural Stiffness

To identify the structural stiffness function $k(\lambda)$, the tensile and compression experiment is conducted. A fabricated one-segment soft continuum robot is clamped and stretched at a velocity of 0.5 mm/s by a universal testing machine (Instron 68SC-2, USA). The elastic force F_e of each soft actuator is then calculated by the following force equilibrium equation $F_e = F_m/3 - F_g$, where F_m and F_g are forces applied by the testing machine and the gravity, respectively. The force-displacement curve of each soft actuator is presented in Fig. 4(a). A quadratic function is used to fit the measured curve whose expression is $F_e = 5,990.4\Delta l^2 + 605.9\Delta l$. Based on the result, the structural stiffness function can be further calculated as $k(\lambda) = 576.94\lambda + 28.9$.

B. Identification of Effective Actuation Diameter

To identify the effective actuation diameter, the actuation force-pressure curve is measured. One side of the soft actuator is vertically clamped. The actuation pressure slowly increases from -30 to 150 kPa, and the corresponding length of the soft actuator l is measured by a motion capture system. The actuation force is calculated by the following force equilibrium equation $F_a = F_e - F_g$, where F_e and F_g are the elastic force and the gravitational force, respectively. The curve of pressures and actuation forces is shown in Fig. 4(b), and the effective actuation area equals the estimated slope. Based on the experimental result, the effective actuation diameter is determined as $D_{\text{eff}} = 8.087$ mm.

C. Identification of Cross-Sectional Diameter

To identify the cross-sectional diameter, a static loading experiment is conducted. As depicted in Fig. 4(c), one side of the soft actuator is horizontally clamped without actuation. In this case, the bending deformation of this soft actuator is generated by the self-weight and the end load, and the stretch ratio equals 1. The vertical displacement of the end is measured as $\Delta z = 34.35$ mm by the motion capture system. Then, the identification of the cross-sectional diameter can be formulated as an optimization problem as follows:

$$\begin{aligned} &\min_{D_a} \left\| q_{6n+3} - \Delta z \right\|^2 \\ &\text{s.t.} \mathbf{Q}_e\left(\mathbf{q}\right) - \mathbf{Q}_g\left(\mathbf{q}\right) - \mathbf{Q}_f\left(\mathbf{q}\right) = \mathbf{0}. \end{aligned} \tag{31}$$

q_{6n+3} refers to the $(6n+3)$th element of the nodal coordinate $\mathbf{q}$, which is also the component of the end effector's global position on the z-axis. For this optimization problem, the number of ANCF elements is set as 20 to ensure the prediction accuracy. The constrained optimization problem is iteratively solved by the bisection method, and then the cross-sectional diameter is determined as $D_a = 17.90$ mm.

D. Determination of ANCF Element Number

Higher degrees of freedom ensure higher accuracy but inevitably sacrifice computational efficiency. To achieve an appropriate balance between these two aspects, the presented method determines the optimal number of ANCF elements through the convergence experiment under extreme actuation forces. This approach ensures sufficient prediction accuracy and significant

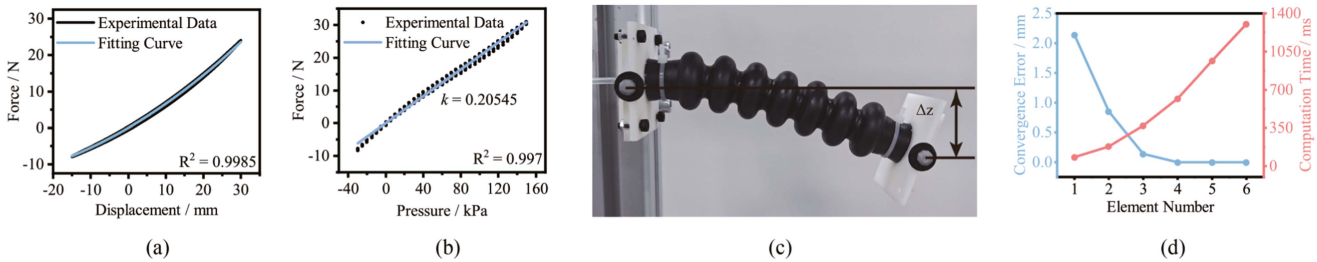

Fig. 4. (a) Result of the structural stiffness identification experiment. (b) Result of the effective actuation diameter identification experiment. (c) Experimental setup of the cross-diameter identification experiment. (d) Relationship among element numbers, convergence errors (blue curve), and the computation times (red curve).

reductions in computational time compared with conventional FEM methods. First, the end-effect position of the one-segment soft continuum robot is calculated when the number of ANCF elements is set as 20 and one soft actuator is inflated to 150 kPa. Since the element number is large enough to ensure the prediction accuracy, the calculated end-effect position is viewed as the ground truth. Then, different element numbers (ranging from 1 to 6) are tested. The convergence error and the computation time are applied as evaluation criteria. As shown in Fig. 4(d), the convergence errors demonstrate a decreasing trend as the element number increases. However, this improvement tends to plateau when the element number exceeds 4. Conversely, the computation time exhibits a steady increase with an increasing number of elements. Therefore, the element number is determined as $n = 4$.

VI. Validation Experiment

To validate the developed kinetostatic model, two experiments are conducted in terms of end-effector position prediction and feedforward trajectory tracking. The end-effector position prediction experiment is used to validate the forward kinetostatic mapping, and the motion control experiment is used to validate the inverse kinetostatic mapping.

A. Experimental Setup

The experimental setup is shown in Fig. 5. The one-segment and two-segment soft continuum robots are vertically clamped. Three reflective markers are attached on the upper base so that both positions and orientations of the end-effector can be measured by the motion capture system (Prime 13, OptiTrack, USA). The motion capture system is calibrated by repeatedly waving a calibration wand with preset markers. Then, the captured data points are used to calculate the position and orientation of each camera. The position accuracy of the motion capture system is 0.15 mm, which is sufficient for the experiment. Electronic pressure regulators (QB1XANEEN100P400KPG, Proportion-Air) and the control module (MicroLabBox-DS1202, dSPACE, USA) are used to regulate the actuation pressures. The forward and inverse kinetostatic problems both are calculated by MATLAB on a PC with AMD Ryzen 7 3700X processor and 32 GB RAM.

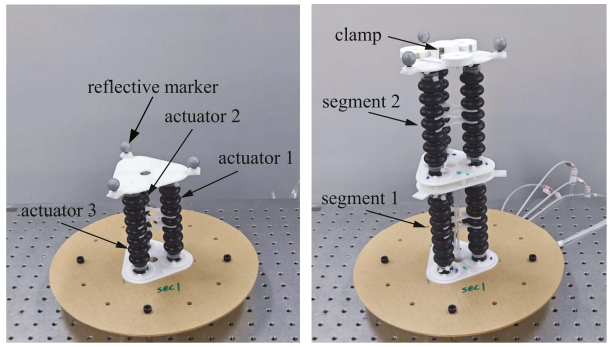

Fig. 5. Experimental setup of the validation experiments for (a) one-segment and (b) two-segment soft continuum robots. Three reflective markers are attached on the upper base to measure the global position. A clamp and weights are used to apply downward force to the end-effector.

B. End-Effector Position Prediction

For the one-segment soft continuum robot, the workspace boundaries are selected to validate the forward kinetostatic model. To prevent damage to soft actuators, the maximum value $P_{\max}$ and the minimum value $P_{\min}$ of the applied pressure are set to 150 and -50 kPa, respectively. Different weights (i.e., 0 g, 50 g, and 100 g) are attached to the end-effector. The total 18 actuation schemes are described as follows.

1) One soft actuator is evenly inflated from $P_{\min}$ to $P_{\max}$, while the actuation pressures of the other two soft actuators are maintained at extreme pressures ($P_{\min}$ or $P_{\max}$).
2) Two soft actuators are evenly inflated from $P_{\min}$ to $P_{\max}$, while the actuation pressure of the remaining soft actuator is maintained at extreme pressures ($P_{\min}$ or $P_{\max}$).

The predicted and measured workspace boundaries under different weights are presented in Fig. 6(a)–(c). The predicted workspace boundaries achieve good consistency with the measured workspace boundaries for all conditions. Besides, the position error distributions of different weight conditions are shown in Fig. 6(d). The root mean square errors (RMSEs) are 5.43 mm for 0 g weight, 5.93 mm for 50 g weight, and 6.25 mm for 100 g weight, respectively. Moreover, the maximum prediction errors are 12.31 mm for 0 g weight, 12.98 mm for 50 g weight, and 12.56 mm for 100 g weight, respectively.

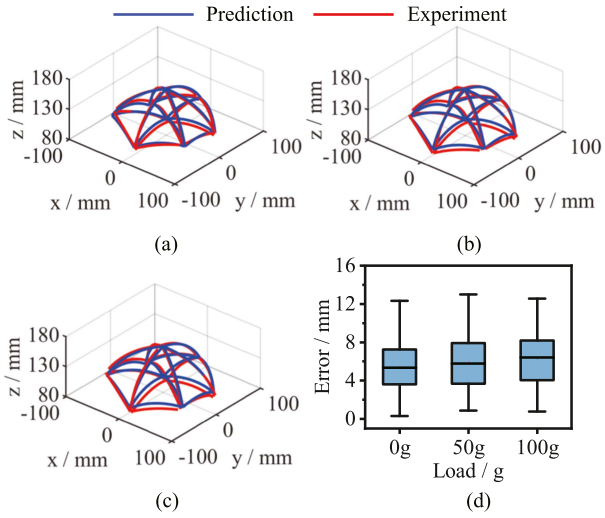

Fig. 6. Predicted and measured workspace boundaries of the one-segment continuum robot with (a) 0 g weight, (b) 50 g weight, and (c) 100 g weight. (d) Distribution of position errors under three weight conditions.

For the two-segment soft continuum robot, because of the high degree of freedom and the structural symmetry, 4 representative trajectories are selected to validate the forward kinetostatic model. To prevent damage to soft actuators, the maximum value $P_{\max}$ and the minimum value $P_{\min}$ of the applied pressure are set to 120 kPa and -50 kPa, respectively. For the sake of brevity, the abbreviation siaj is used to denote the jth soft actuator of the ith segment. The actuation schemes are described as follows.

1) s1a1 and s2a1 are inflated from $P_{\min}$ to $P_{\max}$.
2) s1a1 and s2a2 are inflated from $P_{\min}$ to $P_{\max}$.
3) s1a1, s2a1, and s2a2 are inflated from $P_{\min}$ to $P_{\max}$.
4) s1a1, s2a2, and s2a3 are inflated from $P_{\min}$ to $P_{\max}$.

The actuation pressure of remaining actuators remains 0 kPa. The comparisons between captured and prediction configurations and their prediction errors are presented in Fig. 7. The experimental results suggest that prediction errors are relatively small (below 2.5% of the robot length) under positive actuation pressures.

C. Feedforward Trajectory Tracking

For the one-segment soft continuum robot, five trajectories are selected: a space spiral curve, a space rose curve, a planar circle curve, a planar spiral curve, and a planar rose curve. In addition, the applied weights are 0 g, 50 g, and 100 g. The experimental results, including measured trajectories and tracking error distributions, are shown in Fig. 8. The comparison between the captured configurations and the simulated configurations is shown in Supplementary Video S1. Measure trajectories under different weights highly overlap, and their tracking error distributions are quite similar.

For the two-segment soft continuum robot, both the end-effector positions and the bending angles are controlled. To ensure the elastic stability of the base segment, the applied weights are 0 g, 25 g, 50 g, and 75 g. First, the two-segment soft continuum robot is controlled to track a circle curve with a bending angle of 0°, 10°, or 20°. Fig. 9 shows the experimental results, including experimental images, measured trajectories, position error distributions, and angle error distributions. The position RMSEs under 0 g, 25 g, 50 g, and 75 g weights are 6.21 mm, 6.52 mm, 6.84 mm, and 8.21 mm, respectively. In addition, the angle RMSEs under 0 g, 25 g, 50 g, and 75 g weights are 1.53°, 1.47°, 1.84°, and 2.37°, respectively. Then, the two-segment soft continuum robot is controlled to track a space spiral curve, a space rose curve, a planar spiral curve, and a planar rose curve with 0° bending angle. The experimental results are presented in Fig. 10. Besides, the comparison between the captured configurations and the simulated configurations is shown in Supplementary Video S2. The position RMSEs under 0 g, 25 g, 50 g, and 75 g weights are 4.18 mm, 4.83 mm, 5.07 mm, and 6.42 mm, respectively. In addition, the angle RMSEs under 0 g, 25 g, 50 g, and 75 g weights are 1.71°, 1.59°, 2.35°, and 2.12°, respectively.

D. Discussion

End-effector position prediction and feedforward trajectory tracking experiments both validate the kinetostatic model. Thanks to the decoupling, the kinetostatic models of the one-segment and two-segment soft continuum robots take 0.62 s and 5.32 s to calculate the maximum deformation configurations. Compared to the Cosserat rod-based model [37] with maximum computation time of 5.45 s and 10.96 s, the proposed model achieves a considerable improvement in forward simulation. To demonstrate the tracking accuracy of the presented model, the PCC-based model is also applied to track specified trajectories, and the experimental results are shown in Supplementary Material. The experimental results demonstrate that the ANCF-based model significantly reduces tracking errors, as it effectively accounts for external forces and does not rely on specific deformation assumptions. Meanwhile, Table III shown in Supplementary Material summarizes key performance indicators of approaches found in previous researches and provide a comparison. It is clear that the proposed kinetostatic model achieves high tracking accuracy. Furthermore, Supplementary Material provide a dynamic performance evaluation of the two-segment soft continuum robot. The experimental results indicate that when the drive velocity exceeds 2.67 mm/s, dynamic effects become significant, leading to a noticeable prediction error of the presented kinetostatic model.

This article employs four modeling assumptions to simplify the complex problem of modeling and control of bellow-shaped soft continuum robots. While these assumptions are necessary to facilitate theoretical analysis and initial model development, their validity might be partial in broader practical scenarios. Assumption 1 (constant volume during actuation) is supported by the previous research works [18], [19], [31], which indicates that the chamber volume is only related to the actuation pressure. Meanwhile, it is also reasonable to consider the cross-sectional dimensions as constant (Assumption 3) since they do not change significantly during the stretching or compression process of the actuator. Furthermore, the soft actuators comprising the parallel

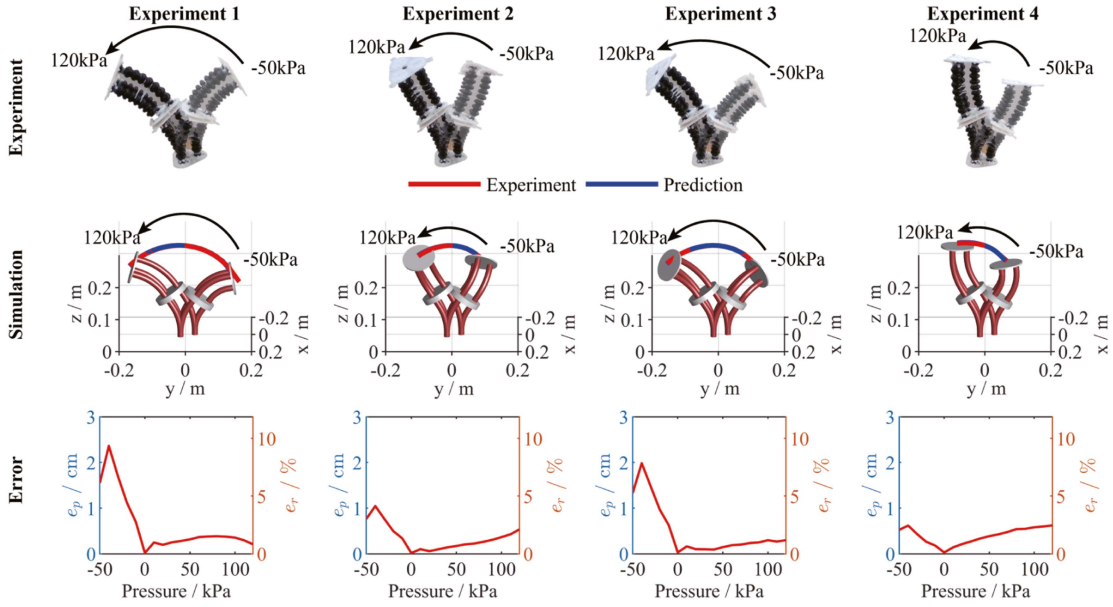

Fig. 7. (Top) Experimental snapshots, (middle) simulation snapshots, and (bottom) position errors of four validation trajectories for the two-segment soft continuum robot.

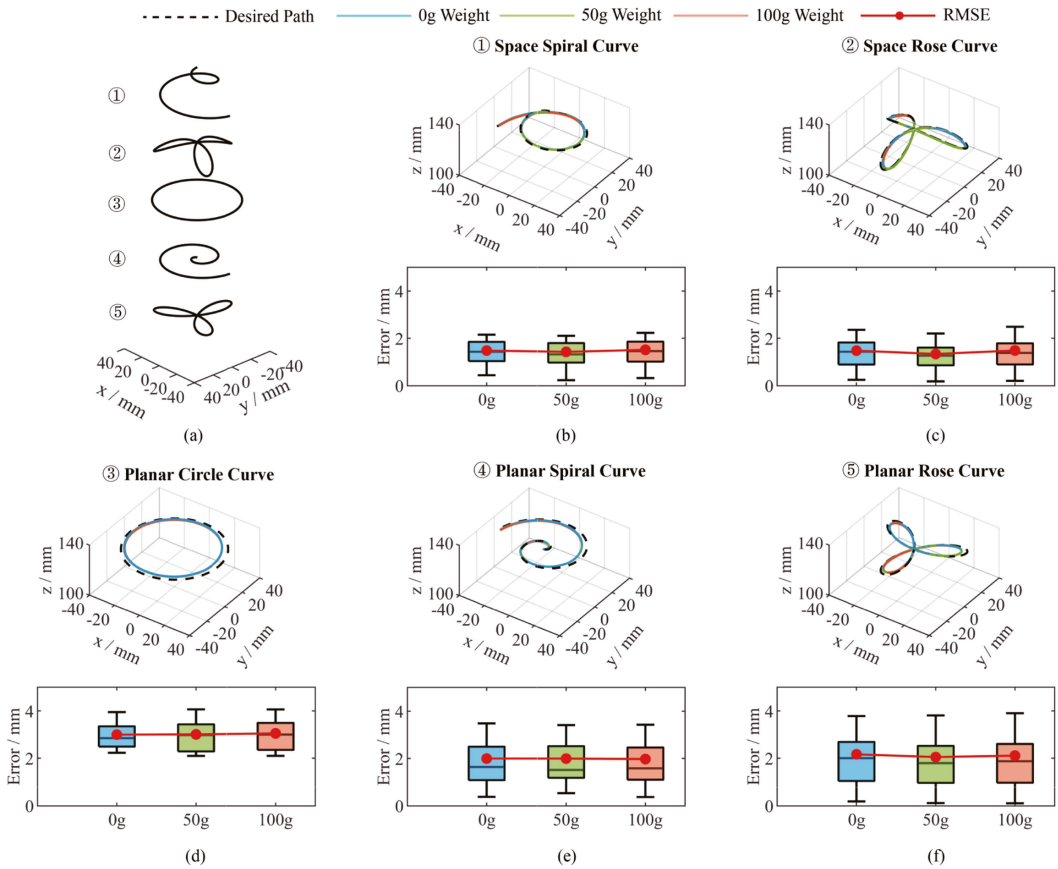

Fig. 8. Trajectory tracking experiments of the one-segment soft continuum robot. (a) Five desired trajectories. Experimental results (top) and position error distributions (below) of tracking the trajectory of (b) space spiral curve, (c) space rose curve, (d) planar circle curve, (e) planar spiral curve, and (f) planar rose curve under different weight conditions.

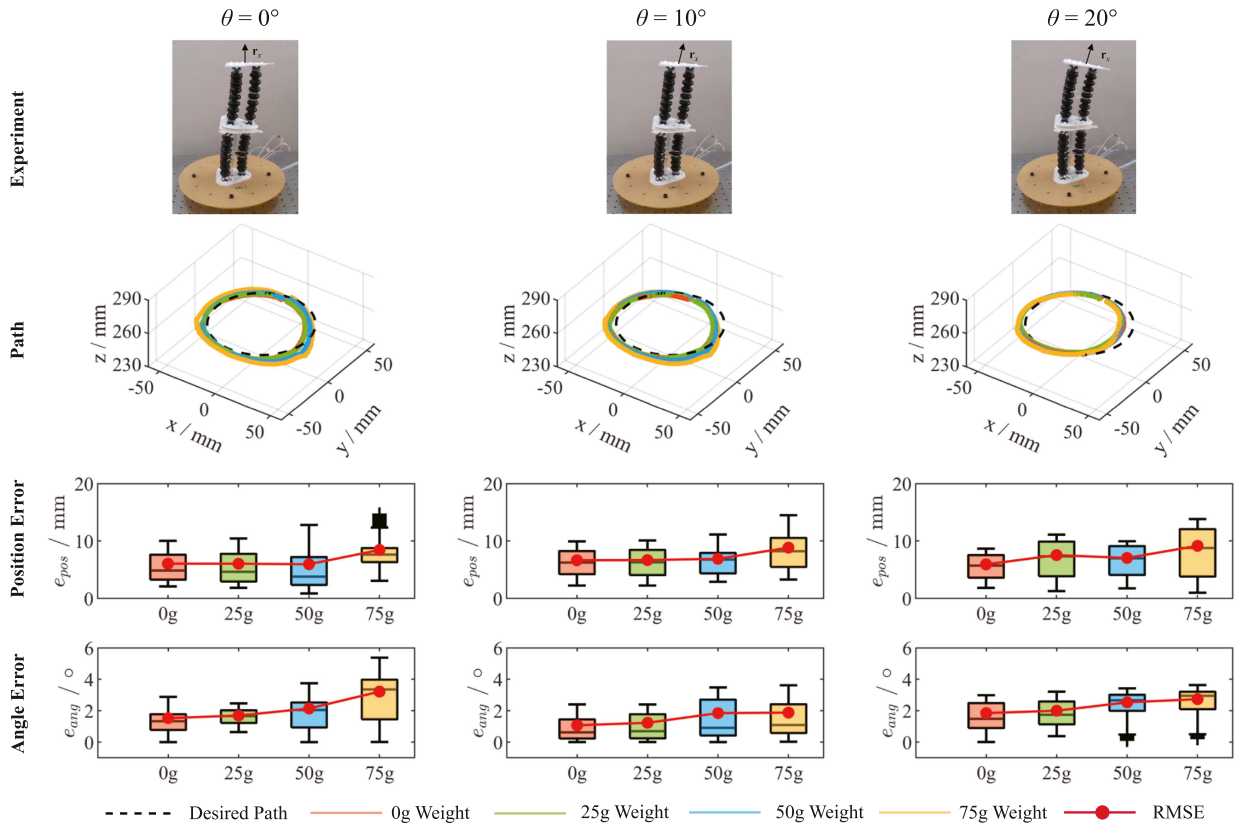

Fig. 9. Experimental snapshots, measured trajectories, position errors, and angle errors when a two-segment soft continuum robot is actuated to track a circle curve with a (left) 0° bending angle, (middle) a 10° bending angle, and (right) a 20° bending angle.

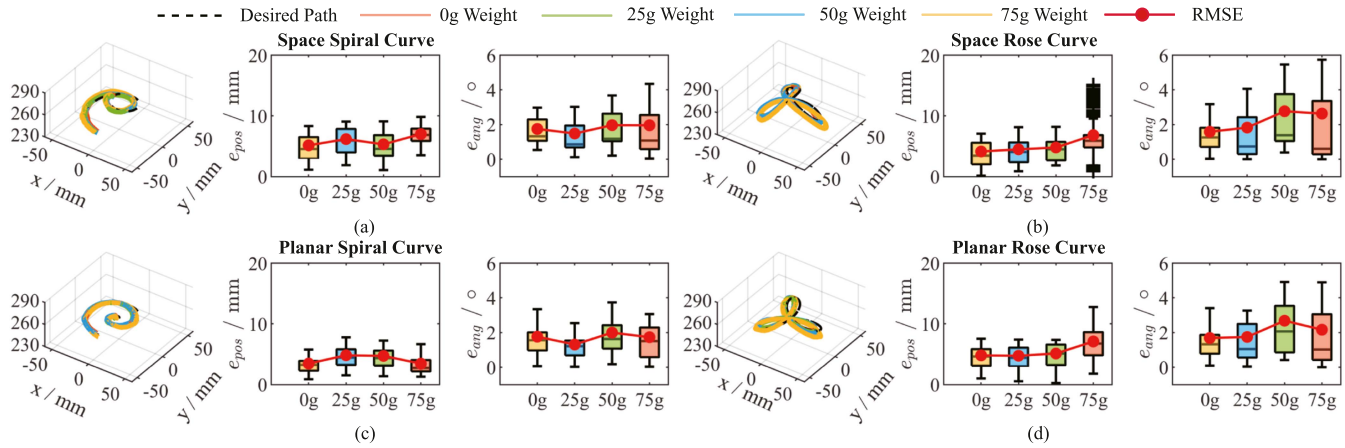

Fig. 10. (Left) Measured trajectories, (middle) position errors, and (right) angle errors when a two-segment soft continuum robot is actuated to track (a) space spiral, (b) space rose curve, (c) planar spiral curve, and (d) planar rose curve with a 0° bending angle.

section can be carefully selected to ensure similar mechanical properties, so Assumption 4 is also reasonable. Therefore, these three assumptions can be generated to other bellow-shaped soft actuators. However, although Assumption 2 (constant effective actuation diameter) is verified in Section V.B, it may only be applicable to the specific actuators employed in this article and cannot be directly generalized to other types of bellow-shaped soft actuators. When applied to other soft continuum robots, the cross-sectional diameters can be expressed as nonlinear functions of the arc length x and identified by experiments.

To improve intrinsic safety, some soft continuum robots are made of softer materials such as Shore hardness 10 A. These materials exhibit more pronounced hyperelasticity compared to the applied robot in this work. In such case, a quadratic curve is insufficient to accurately describe the pressure-deformation relationship, necessitating the use of a higher order polynomial model. Meanwhile, the equation of generalized elastic forces

needs to be derived again based on the used polynomial functions. The remaining part of the modeling and control framework can be applied in the same manner. Furthermore, to extend the presented kinetostatic model to a dynamic model, we intend to derive equations for dynamic forces or employ neural networks to approximate them.

VII. Conclusion

In this work, we propose a kinetostatic model and a corresponding feedforward controller for bellow-shaped soft continuum robots, which consider both the variable curvature configurations and the variable stiffness. To enhance the computational efficiency, two simplifying approaches are applied. The first one is to replace the original bellow-shaped soft actuators with hyperelastic cylinder soft actuators in the calculation process while maintaining the mechanical equivalence. The second approach is to decouple the entire deformation process into the elongation deformation and the bending deformation, averting the analytical derivation of actuation forces. Both approaches avoid the need for volume discretization [38], thus reducing the computational time. With these simplifying approaches, a kinetostatic model is developed based on ANCF theory. Afterwards, the forward and inverse kinetostatic mappings are defined and solved by the numerical solution algorithm. Finally, the developed model is experimentally validated in terms of configuration simulation and feedforward trajectory tracking. Experimental results demonstrate that the model achieves low prediction errors of configuration simulation (3.43 %). Besides, with the feedforward controller, the two-segment soft continuum robot can accurately follow desired trajectories with specified bending angles, where the average position error and angle error are 4.14 mm and 1.58°, respectively.

References

[1] D. Rus and M. T. Tolley, "Design, fabrication and control of soft robots," *Nature*, vol. 521, no. 7553, pp. 467–475, 2015.

[2] O. Yasa et al., "An overview of soft robotics," *Annu. Rev. Control, Robot., Auton. Syst.*, vol. 6, no. 1, pp. 1–29, 2023.

[3] M. Feng, D. Yang, and G. Gu, "High-force fabric-based pneumatic actuators with asymmetric chambers and interference-reinforced structure for soft wearable assistive gloves," *IEEE Robot. Autom. Lett.*, vol. 6, no. 2, pp. 3105–3111, Apr. 2021.

[4] D. Yang, M. Feng, and G. Gu, "High-stroke, high-output-force, fabric-lattice artificial muscles for soft robots," *Adv. Mater.*, vol. 36, no. 2, 2024, Art. no. 2306928.

[5] G. Gu et al., "A soft neuroprosthetic hand providing simultaneous myoelectric control and tactile feedback," *Nature Biomed. Eng.*, vol. 7, no. 4, pp. 589–598, 2023.

[6] N. Zhang et al., "Soft robotic hand with tactile palm-finger coordination," *Nature Commun.*, vol. 16, no. 1, 2025, Art. no. 2395.

[7] M. Feng, D. Yang, L. Ren, G. Wei, and G. Gu, "X-crossing pneumatic artificial muscles," *Sci. Adv.*, vol. 9, no. 38, 2023, Art. no. eadi7133.

[8] Y. Zhang, D. Yang, P. Yan, P. Zhou, J. Zou, and G. Gu, "Inchworm inspired multimodal soft robots with crawling, climbing, and transitioning locomotion," *IEEE Trans. Robot.*, vol. 38, no. 3, pp. 1806–1819, Jun. 2022.

[9] D. Wang et al., "Dexterous electrical-driven soft robots with reconfigurable chiral-lattice foot design," *Nature Commun.*, vol. 14, no. 1, 2023, Art. no. 5067.

[10] M. Runciman, A. Darzi, and G. P. Mylonas, "Soft robotics in minimally invasive surgery," *Soft robotics*, vol. 6, no. 4, pp. 423–443, 2019.

[11] X. Huang, X. Zhu, and G. Gu, "Kinematic modeling and characterization of soft parallel robots," *IEEE Trans. Robot.*, vol. 38, no. 6, pp. 3792–3806, Dec. 2022.

[12] A. A. A. Moghadam, A. Kouzani, K. Torabi, A. Kaynak, and M. Shahinpoor, "Development of a novel soft parallel robot equipped with polymeric artificial muscles," *Smart Mater. Structures*, vol. 24, no. 3, 2015, Art. no. 035017.

[13] D. Drotman, M. Ishida, S. Jadhav, and M. T. Tolley, "Application-driven design of soft, 3-D printed, pneumatic actuators with bellows," *IEEE/ASME Trans. Mechatron.*, vol. 24, no. 1, pp. 78–87, Feb. 2019.

[14] J. A. Saglia, N. G. Tsagarakis, J. S. Dai, and D. G. Caldwell, "Control strategies for ankle rehabilitation using a high performance ankle exerciser," in *Proc. IEEE Int. Conf. Robot. Autom.*, 2010, pp. 2221–2227.

[15] E. Spyrakos-Papastavridis, P. R. N. Childs, and J. S. Dai, "Passivity preservation for variable impedance control of compliant robots," *IEEE/ASME Trans. Mechatron.*, vol. 25, no. 5, pp. 2342–2353, Oct. 2020.

[16] N. Mao, J. Chen, G. Jia, E. Spyrakos-Papastavridis, and J. S. Dai, "Kinetostatics and particle-swarm optimization of vehicle-mounted underactuated metamorphic loading manipulators," *Mechanism Mach. Theory*, vol. 217, 2025, Art. no. 106254.

[17] J. Zou, S. O. Kassim, J. Ren, V. Vaziri, S. S. Aphale, and G. Gu, "A generalized motion control framework of dielectric elastomer actuators: Dynamic modeling, sliding-mode control and experimental evaluation," *IEEE Trans. Robot.*, vol. 40, pp. 919–935, 2024.

[18] F. Chen, Z. Song, S. Chen, G. Gu, and X. Zhu, "Morphological design for pneumatic soft actuators and robots with desired deformation behavior," *IEEE Trans. Robot.*, vol. 39, no. 6, pp. 4408–4428, Dec. 2023.

[19] G. Fang, C.-D. Matte, R. B. N. Scharff, T.-H. Kwok, and C. C. L. Wang, "Kinematics of soft robots by geometric computing," *IEEE Trans. Robot.*, vol. 36, no. 4, pp. 1272–1286, Aug. 2020.

[20] H. Wang, B. Yang, Y. Liu, W. Chen, X. Liang, and R. Pfeifer, "Visual servoing of soft robot manipulator in constrained environments with an adaptive controller," *IEEE/ASME Trans. Mechatron.*, vol. 22, no. 1, pp. 41–50, Feb. 2017.

[21] G. Olson, S. Chow, A. Nicolai, C. Branyan, G. Hollinger, and Y. Mengüç, "A generalizable equilibrium model for bending soft arms with longitudinal actuators," *Int. J. Robot. Res.*, vol. 40, no. 1, pp. 148–177, 2021.

[22] P. S. Gonthina, A. D. Kapadia, I. S. Godage, and I. D. Walker, "Modeling variable curvature parallel continuum robots using Euler curves," in *Proc. Int. Conf. Robot. Autom.*, 2019, pp. 1679–1685.

[23] I. Singh, Y. Amara, A. Melingui, P. Mani Pathak, and R. Merzouki, "Modeling of continuum manipulators using Pythagorean hodograph curves," *Soft Robot.*, vol. 5, no. 4, pp. 425–442, 2018.

[24] D. C. Rucker and R. J. Webster III, "Statics and dynamics of continuum robots with general tendon routing and external loading," *IEEE Trans. Robot.*, vol. 27, no. 6, pp. 1033–1044, Dec. 2011.

[25] K. Oliver-Butler, J. Till, and C. Rucker, "Continuum robot stiffness under external loads and prescribed tendon displacements," *IEEE Trans. Robot.*, vol. 35, no. 2, pp. 403–419, Apr. 2019.

[26] C. Meier, A. Popp, and W. A. Wall, "Geometrically exact finite element formulations for slender beams: Kirchhoff–Love theory versus Simo–Reissner theory," *Arch. Comput. Methods Eng.*, vol. 26, no. 1, pp. 163–243, 2019.

[27] C. Armanini, F. Boyer, A. T. Mathew, C. Duriez, and F. Renda, "Soft robots modeling: A structured overview," *IEEE Trans. Robot.*, vol. 39, no. 3, pp. 1728–1748, Jun. 2023.

[28] F. Renda, A. Mathew, and D. F. Talegon, "Dynamics and control of soft robots with implicit strain parametrization," *IEEE Robot. Autom. Lett.*, vol. 9, no. 3, pp. 2782–2789, Mar. 2024.

[29] J. Gerstmayr, H. Sugiyama, and A. Mikkola, "Review on the absolute nodal coordinate formulation for large deformation analysis of multibody systems," *J. Comput. Nonlinear Dyn.*, vol. 8, no. 3, 2013, Art. no. 031016.

[30] A. A. Shabana and R. Y. Yakoub, "Three dimensional absolute nodal coordinate formulation for beam elements: Theory," *J. Mech. Des.*, vol. 123, no. 4, pp. 606–613, 2001.

[31] J. Liang, X. Huang, K. Luo, Z. Song, Y. Yang, and F. Chen, "Design and kinematic modeling of a pneumatic soft bellow-type wrist," *IEEE Robot. Automat. Lett.*, vol. 9, no. 7, pp. 6312–6319, Jul. 2024.

[32] A. A. Shabana, "Definition of ANCF finite elements," *J. Comput. Nonlinear Dyn.*, vol. 10, no. 5, 2015, Art. no. 054506.

[33] S. Kulkarni and A. A. Shabana, "Spatial ANCF/CRBF beam elements," *Acta Mechanica*, vol. 230, pp. 929–952, 2019.

[34] X. Huang, J. Zou, and G. Gu, "Kinematic modeling and control of variable curvature soft continuum robots," *IEEE/ASME Trans. Mechatron.*, vol. 26, no. 6, pp. 3175–3185, Dec. 2021.

[35] J. J. Moré, "The Levenberg-Marquardt algorithm: Implementation and theory," in *Proc. Numer. Anal.: Proc. Biennial Conf.* Dundee, 2006, Jul. 28, pp. 105–116.
[36] A. Garriga-Casanovas and F. Rodriguez y Baena, "Kinematics of continuum robots with constant curvature bending and extension capabilities," *J. Mech. Robot.*, vol. 11, no. 1, 2018, Art. no. 011010.
[37] J. Shi, A. Shariati, S.-A. Abad, Y. Liu, J. S. Dai, and H. A. Wurdemann, "Stiffness modelling and analysis of soft fluidic-driven robots using lie theory," *Int. J. Robot. Res.*, vol. 43, no. 3, pp. 354–384, 2024.
[38] Q. Xu and J. Liu, "Effective enhanced model for a large deformable soft pneumatic actuator," *Acta Mechanica Sinica*, vol. 36, pp. 245–255, 2020.

Yu Rong received the B.E. degree in mechatronic engineering from Northwestern Polytechnical University, Xi'an, China, in 2019. He is currently working toward the Ph.D. degree in mechatronic engineering with Shanghai Jiao Tong University, Shanghai, China.

His research interests include modeling and control of soft continuum robots.

Guoying Gu (Senior Member, IEEE) received the B.E. degree (Hons.) in electronic science and technology and the Ph.D. degree (Hons.) in mechatronic engineering from Shanghai Jiao Tong University, Shanghai, China, in 2006 and 2012, respectively.

He was a Humboldt Fellow with the University of Oldenburg, Oldenburg, Germany, and was a Visiting Scholar with the Massachusetts Institute of Technology, Cambridge, MA, USA, the National University of Singapore, Singapore, and Concordia University, Montreal, QC, Canada. He is currently a Distinguished Professor with the School of Mechanical Engineering, Shanghai Jiao Tong University. He has authored or coauthored more than 150 publications, including articles in *Science, Science Robotics*, *Nature Biomedical Engineering*, *Nature Reviews Materials*, *Nature Materials*, *Nature Communications*, *Science Advances*, *Advanced Materials*, *Soft Robotics*, Science China series, the IEEE/ASME Transactions journals, book chapters, and international conference proceedings. His research interests include soft robotics, bioinspired and wearable robots, and smart materials for sensing, actuation, and motion control.

Dr. Gu was the recipient of the National Science Fund for Distinguished Young Scholars and the XPLORER Prize. He is currently an Associate Editor for *Soft Robotics*, *Soft Science*, and IEEE TRANSACTIONS ON AUTOMATION SCIENCE AND ENGINEERING, and was an Associate Editor for IEEE TRANSACTIONS ON ROBOTICS and IEEE ROBOTICS AND AUTOMATION LETTERS.